The Astrophysical Journal, 668: L179–L182, 2007 October 20

A *SPITZER* SEARCH FOR WATER IN THE TRANSITING EXOPLANET HD 189733b

David Ehrenreich, Guillaume Hébrard, Alain Lecavelier des Etangs, David K. Sing, Jean-Michel Désert, François Bouchy, Roger Ferlet, and Alfred Vidal-Madjar
Institut d'astrophysique de Paris, CNRS (UMR 7095), Université Pierre et Marie Curie, 98 bis boulevard Arago, 75014 Paris, France
Received 2007 March 19; accepted 2007 August 27; published 2007 October 2

ABSTRACT

We present *Spitzer Space Telescope* observations of the extrasolar planet HD 189733b primary transit, obtained simultaneously at 3.6 and 5.8 μm with the Infrared Array Camera. The system parameters, including planetary radius, stellar radius, and impact parameter, are derived from fits to the transit light curves at both wavelengths. We measure two consistent planet-to-star radius ratios, $(R_p/R_\star)_{3.6\,\mu\mathrm{m}} = 0.1560 \pm 0.0008(\mathrm{stat}) \pm 0.0002(\mathrm{syst})$ and $(R_p/R_\star)_{5.8\,\mu\mathrm{m}} = 0.1541 \pm 0.0009(\mathrm{stat}) \pm 0.0009(\mathrm{syst})$, which include both the random and systematic errors in the transit baseline. Although planet radii are determined at 1% accuracy, if all uncertainties are taken into account, the resulting error bars are still too large to allow for the detection of atmospheric constituents like water vapor. This illustrates the need to observe multiple transits with the longest possible out-of-transit baseline, in order to achieve the precision required by transmission spectroscopy of giant extrasolar planets.

Subject headings: planetary systems — stars: individual (HD 189733)

1. INTRODUCTION

During a planetary transit, the eclipsed light from the star filters through the atmospheric limb of the planet. Transmission spectroscopy of this light leads to the detection and probing of the deep and upper-escaping atmospheres of HD 209458b (Charbonneau et al. 2002; Vidal-Madjar et al. 2003, 2004; Ballester et al. 2007). Richardson et al. (2006) obtained the first infrared (IR) transit measurement for this planet and found its radius at 24 μm consistent with the visible radius. On the basis of planetary radius measurements by Knutson et al. (2007a) at optical wavelengths, Barman (2007) claimed the identification of water in the planet atmosphere.

HD 189733b, discovered by Bouchy et al. (2005), is orbiting a small, close, and bright main-sequence K star, thus giving the deepest transit occultation ever detected (~2.5%). The planet has a mass $M_p = 1.13\ M_J$ and its radius in the visible is $R_p = 1.16\ R_J$ (Bakos et al. 2006; Winn et al. 2007). Fortney & Marley (2007) suggested a possible water detection in this planet, yielding from *Spitzer* observations of an antitransit, whereas Knutson et al. (2007b) obtained the planet-to-star radius ratio at 8 μm and found $(R_p/R_\star)_{8\,\mu\mathrm{m}} = 0.1545 \pm 0.0002$.

Here we describe the *Spitzer* observations collected during the primary transit of HD 189733b in order to measure its radius at two different IR wavelengths and search for atmospheric water (H_2O). Models of the IR transmission spectrum of this planet (Tinetti et al. 2007a, 2007b) have shown that *Spitzer* is well suited to probe the planet atmospheric composition, in particular by comparing two photometric bands, centered at 3.6 and 5.8 μm. The absorption by H_2O should give a difference in the spectral ratios measured at those two wavelengths of $\Delta_{\Re'}(H_2O) \equiv (\Re'_{5.8\,\mu\mathrm{m}} - \Re'_{3.6\,\mu\mathrm{m}})/\Re'_{3.6\,\mu\mathrm{m}} \sim 1.7\%$–$3.4\%$, depending on the set of H_2O absorption cross section coefficients used for the calculation, and where $\Re' \approx (R_p/R_\star)^2$, as defined by Brown (2001). This corresponds to a predicted planetary radius relative difference due to absorption by H_2O of $\Delta_R(H_2O) \sim 0.85\%$–$1.7\%$.

2. OBSERVATIONS

We observed HD 189733 on 2006 October 31, during a primary transit of its planet with the Infrared Array Camera (IRAC; Fazio et al. 2004). Our 4.5 hr observations covers the 1.8 hr transit of HD 189733b. We used only one IRAC channel pair to avoid repointing the telescope during the observations: the 0.75 μm wide channel 1 centered on 3.6 μm, and the 1.42 μm wide channel 3 centered on 5.8 μm. We did not dither the pointing in order to keep the source on a particular position of the detector and increase the photometric accuracy.

The observations were split in 1936 consecutive subexposures, each integrated over 0.4 and 2 s (frame times) for channels 1 and 3, respectively. The short exposure times in IRAC "stellar mode" avoid the saturation of the detector due to HD 189733, a $K = 5.5$ mag star. We used the flat-fielded, cosmic-ray–corrected, and flux-calibrated data files provided by the *Spitzer* pipeline.

3. DATA ANALYSIS

3.1. *Photometry and Background*

To obtain a transit light curve from the two-dimensional 1936 images, we calculate a weighted aperture photometry by summing the weighted background-subtracted flux on each pixel within an aperture of given radius r (Horne 1986; Naylor 1998). The optimal weighting on a pixel is P/σ^2, where P and σ are the values of the point-spread function (PSF) and photon noise for this pixel. The PSF is estimated in each channel and for each pixel as the median of the background-subtracted fluxes. Finally, the estimated error on the weighted integrated flux is calculated as the square root of the weighted photon-noise quadratic sum; it remains a constant throughout the time series.

To estimate the sky and instrumental background for each exposure, we calculated the mean value of the image in an annulus centered on the star with inner and outer radii of 16 and 18 pixels, respectively. Different ring sizes were tested to check that (1) the stellar PSF does not contaminate the background and (2) other field stars contribution is minimized. Typical background estimates are ~0.05 and 0.1–0.2 mJy pixel^{-1} in channels 1 and 3, respectively. They are $\sim 10^4$ times less than stellar flux integrated over the 113 pixel photometric aperture.

The initial weighted flux time series were extracted with an aperture radius $r = 6$ pixels. The raw weighted light curves in channels 1 and 3 are plotted in Figure 1. Beyond the main trend due to the expected planetary transit, with an occultation depth of more than 2% during about 6500 s, additional effects pollute

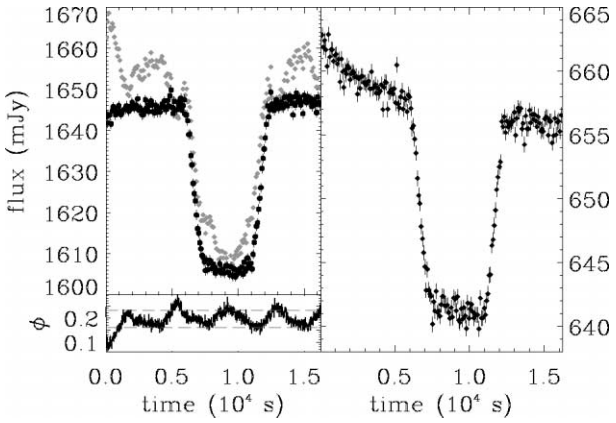

FIG. 1.—Weighted light curves in channel 1 at 3.6 μm (*left*) and channel 3 at 5.8 μm (*right*). Data are rebinned by 10. The raw light curve at 3.6 μm (*gray diamonds*) has to be corrected for large fluctuations correlated to the "pixel phase," plotted in the lower left panel. Those exposures with extreme pixel phases (beyond the dashed lines) are rejected. The corrected light curve is overplotted as black circles in the upper panel.

the signal. In both channels, there is a strong decrease of the flux during the first ~1000 s of observations. Most noticeable in channel 1 at 3.6 μm, the star is close to nominal saturation limits and the light curve presents large fluctuations, attributed to the "pixel-phase effect." A close look to the 2D images obtained in channel 3 at 5.8 μm reveals a contamination of the photometry caused by the "bandwidth effect." The light-curve baseline is also affected in this channel by a decreasing drift. These effects and their corrections are now further detailed.

3.2. *Instrumental Artifacts*

Saturation.—The flux of HD 189733 is 1700 mJy at 3.6 μm. This is about twice the maximum recommended (and conservative) point source value for a frame time of 0.4 s in stellar mode.[1] Looking into the raw data from channel 1, we found that the brightest pixel of the stellar PSF is above the detector array saturating value ($DN = 30{,}000$) *only* during the ~100 first subexposures. Those are already discarded for the data reduction. In the following subexposures, the flux remains below the saturation limit, in the linear regime.

Pixel-phase effect at 3.6 μm.—The telescope jitter and intrapixel sensitivity variations for the observation of a bright star are likely responsible for the large fluctuations seen in the light curve obtained at 3.6 μm in channel 1. These fluctuations are correlated to the pixel-phase variation, whose effect is most severe in channel 1. A description of this effect and a correction method are given in the IRAC data handbook (Reach et al. 2006, p. 50). The method, also reported by Morales-Calderón et al. (2006), consists in calculating a pixel-phase dependent correction on the flux, $F_w^{\rm cor} = F_w\,[1 + k\,(1/2\pi - \phi)]^{-1}$, where the pixel phase is $\phi = [(x - x_0)^2 + (y - y_0)^2]^{1/2}$, (x, y) is the centroid of the point source, and x_0 and y_0 are the integer pixel numbers containing the source centroid. The optimized correction is determined by iteratively fitting the out-of-transit flux baseline. The pixel phase variations and the raw and corrected light curves are plotted in Figure 1 (*left*). The relative difference introduced by this correction on the value of $(R_p/R_\star)_{3.6\,\mu\rm m}$ can be estimated to $\Delta_R^{3.6\,\mu\rm m}(\text{phase}) \sim 2\%$–$3\%$.

Bandwidth effect at 5.8 μm.—The bandwidth effect reportedly affects those IRAC channels fitted with detector arrays made of arsenic-doped silicon (Si:As), such as channel 3. The IRAC data handbook (Reach et al. 2006, p. 24) describes it as decaying echoes 4, 8, and 12 columns to the right of a bright or saturated pixel. HD 189733 is no brighter than 700 mJy at 5.8 μm, whereas the maximum unsaturated point source brightness at this wavelength and for 2 s frame time is 1400 mJy.[1] Yet the pixel located four columns to the right of the stellar maximum is anomalously bright in all exposures and appears as a peak in the wing of the stellar PSF, ~2–3 times brighter than closer-to-the-centroid adjacent pixels. Therefore, we rejected this suspicious pixel from the aperture photometry integration, as recommended by IRAC status reports.[2] This decreases the value obtained for $(R_p/R_\star)_{5.8\,\mu\rm m}$, and the relative difference between the corrected and uncorrected values is $\Delta_R^{5.8\,\mu\rm m}(\text{band}) \sim 1\%$. The bandwidth effect could typically lead to obtaining a planetary radius systematically larger at 5.8 than at 3.6 μm and mimic an absorption due to atmospheric water, hence leading to a false detection.

Drift of the flux at 5.8 μm.—A nonlinear decreasing drift can be seen in the channel 3 light curve (Fig. 1, *right*). After steeply decreasing, the drift seems to set a nearly linear trend after 2500 s. This gives us the choice of dropping the exposures before that time and linearly fitting the out-of-transit baseline after, or keeping most of the exposures at the beginning of the observations and performing either a quadratic or exponential fit to the baseline. We tested the influence of both the polynomial fitted to the baseline and the number of exposures dropped from the beginning of the observations on the system parameters yielding from the fitting procedure. To this purpose, the time t_s defining the start of the fit was set as a free parameter. For consistency, the same tests were performed in channel 1, and their results are plotted in Figure 2. A large dispersion of values is obtained, especially for $(R_p/R_\star)_{5.8\,\mu\rm m}$ in channel 3.

[1] See http://ssc.spitzer.caltech.edu/irac/sat.html.

[2] See the 2005 October and December IRAC status reports at https://lists.ipac.caltech.edu/mailman/htdig/irac-ig.

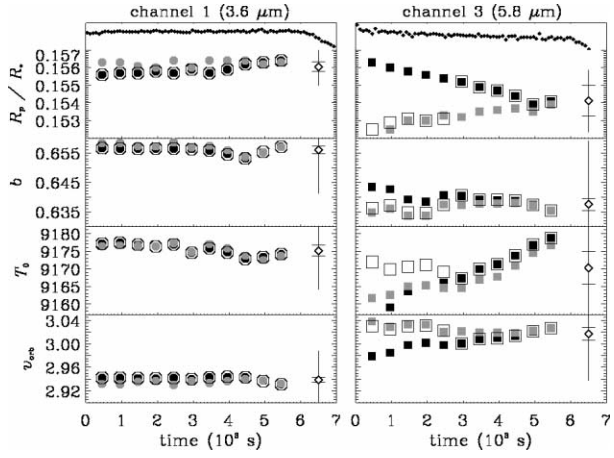

FIG. 2.—System parameters obtained in channels 1 (*left*) and 3 (*right*), as a function of the time from which the transit light curve is fitted. The light curves in both channels are plotted in the upper panels until the ingress. The parameters shown are, from top to bottom, $R_p/R_\star$, b, T_0, and $v_{\rm orb}$. To correct for the decreasing drift in channel 3, the transit light-curve model can include a linear (*black*), quadratic (*gray*), or exponential (*open symbols*) out-of-transit baseline. For consistency, we also applied these fitting tests to channel 1. The dispersion observed in the results is accounted for by choosing the mean of each sample (*open diamonds*) and adding a systematic uncertainty equal to the standard deviation in each sample. The error bar represented in each panel accounts for the statistical *and* systematic errors. The contribution of the systematics is indicated by the horizontal bars.

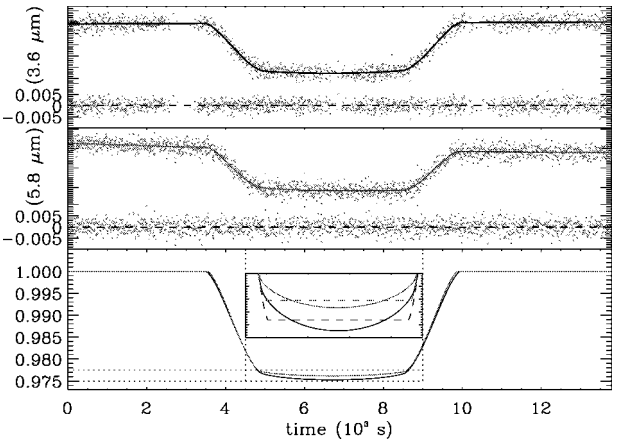

FIG. 3.—Final light curves of HD 189733 during the 2006 October 31 transit at 3.6 (*top*) and 5.8 μm (*middle*). Fits to the light curves (*thick lines*) are calculated from the system parameters given in Table 1. The residuals are shown below each fitted light curve. The lower panel shows a comparison between the two fits. The inlet contains a zoom on the transit bottom, where our best fits obtained without limb darkening are superimposed (*dashed lines*).

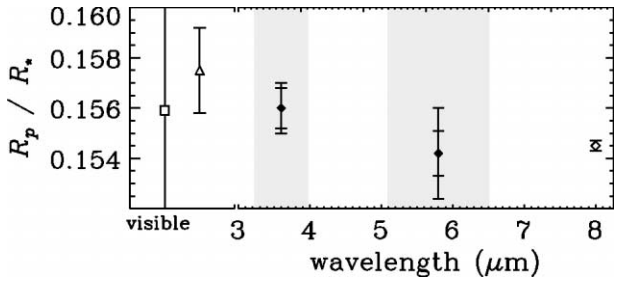

FIG. 4.—Radius of the planet as a function of wavelength, expressed in stellar radii. The two measurements at 3.6 and 5.8 μm are represented (*filled diamonds*) in the near IR. Both IRAC bandpasses are also indicated (*gray areas*). Previous measurements in the visible (Bakos et al. 2006, *square*; Winn et al. 2007, *triangle*) and in the IR (Knutson et al. (2007b, *open diamond*) are shown for comparison.

Depending on the fit parameters, the dispersions obtained are $\Delta_R^{3.6\,\mu m}(\text{drift}) \sim 0.1\%$ and $\Delta_R^{5.8\,\mu m}(\text{drift}) \sim 0.6\%$ at 3.6 and 5.8 μm, respectively. The limited knowledge of the baseline exact level during the transit introduces systematic uncertainties in the determination of the system parameters. These uncertainties are further taken into account as systematic errors.

3.3. *Determination of the System Parameters*

Selection of subexposures.—We made a selection within the 1936 subexposures to obtain the best possible photometry. Subexposures where the aperture contains at least 1 pixel flagged by the *Spitzer* pipeline are removed from our time series. We did not apply such selection to one particular pixel always present in the wing of the PSF in channel 1: it is systematically flagged as having a "photometric accuracy unacceptably low," which is verified when compared to adjacent pixels. However, we found no significant differences when including or excluding it from the aperture photometry. We also removed the dozen subexposures in each channel where the integrated photometry of HD 189733 presents strong and isolated variations. Finally, we kept in channel 1 the exposures where the pixel phase was in the range $0.16 < \phi < 0.23$ (see Fig. 1) and rejected the others in order to minimize the influence of residuals from the correction for the pixel-phase effect. As a result, when cutting out the first 500 s of data after the beginning of the observations, we consider 75% and 96% of the total number of exposures in channels 1 and 3, respectively.

Fitting the transit light curves.—The transit light curves at 3.6 and 5.8 μm are fitted with a procedure based on the analytical model of Mandel & Agol (2002), which includes the effect of limb darkening. The procedure is able to fit either linear, quadratic, or exponential baselines. The resulting parameters of the fit at each wavelength are the planet-to-star radius ratio $R_p/R_\star$, the impact parameter b in units of stellar radii, the orbital velocity $v_{\rm orb}$ in units of stellar radii which, because the planet orbital period is known to high accuracy (2.218574 days, according to Hébrard & Lecavelier des Etangs 2006), can be converted into $R_\star M_\star^{-1/3}$, where $M_\star$ is the stellar mass, and the heliocentric transit central time T_0. The best fits obtained are plotted in Figure 3.

Limb-darkening effect.—The contribution of limb darkening to the transit light curve is calculated using a nonlinear limb-darkening law (Mandel & Algol 2002) that has four wavelength-dependent coefficients. These coefficients were fitted using a Kurucz (2006) stellar model ($T_{\rm eff} = 5000$ K, $\log g = 4.5$, solar abundance), which closely matched the observed parameters of HD 189733, at 17 different angles from center to limb. The stellar model was convolved, at each angle, with the IRAC photometric bandpasses before fitting the nonlinear law. We found the coefficients C_1, C_2, C_3, and C_4 of the law to be 0.6023, -0.5110, 0.4655, and -0.1752 at 3.6 μm, and 0.7137, -1.0720, 1.0515, and -0.3825 at 5.8 μm. The uncertainty in the limb-darkening coefficients has no impact on the results. However, the uncertainty in the impact parameter introduces an uncertainty in the limb-darkening amplitude and therefore an uncertainty in the measured planetary radius. The relative radius difference at 3.6 μm due to the limb-darkening effect is $\Delta_R^{3.6\,\mu m}(\text{limb}) \sim 1\%$ and $\Delta_R^{5.8\,\mu m}(\text{limb}) \sim 0.3\%$ at 3.6 and 5.8 μm, respectively. The limb-darkening effect can be appreciated in the bottom panel of Figure 3.

Statistical error bars.—The statistical error bars on the parameters are calculated with the $\Delta\chi^2$ method described by Hébrard et al. (2002). The quality of the fit is given by the value of χ^2/n, where n is the degree of freedom of the light curve. Assuming we are limited by the photon noise, we find χ^2/n of ~1.5 and 1.3 at 3.6 and 5.8 μm, respectively. We thus scaled the uncertainties larger by factors of $\sqrt{1.5} = 1.22$ and $\sqrt{1.3} = 1.14$ to obtain $\chi^2/n \sim 1$ in both channels. Using various models and starting time for the baseline gives similar χ^2 values, showing that the light curve does not contain enough information to constrain that source of uncertainty.

Systematics.—The effects described above all introduce systematics that are clearly not negligible compared to the predicted radius differences due to atmospheric water, $\Delta_R(\text{H}_2\text{O}) \sim 0.85\%$–$1.7\%$. Limb-darkening effect, introducing $\Delta_R^{3.6\,\mu m}(\text{limb}) \sim 1\%$ in channel 1 and $\Delta_R^{5.8\,\mu m}(\text{limb}) \sim 0.3\%$ in channel 3, is dealt with as described in the previous section. Tests show that we are able to fairly correct for $\Delta_R^{3.6\,\mu m}(\text{phase}) \sim 2\%$ and $\Delta_R^{5.8\,\mu m}(\text{band}) \sim 1\%$. On the other hand, additional uncertainty has to be introduced to properly handle the systematics linked to the drift in the flux seen in channel 3 and, to a lesser extent, in channel 1. Indeed, basing ourselves on the similar reduced χ^2 obtained when fitting the baseline with different polynomials, we cannot choose one of the sets of system parameters rather than another. Besides, in the absence of a "plateau" in the plot of $(R_p/R_\star)_{5.8\,\mu m}$ versus t_s, we cannot either favor one solution based on the time t_s chosen to start the fitting procedure. After removing the solutions cor-

TABLE 1
SYSTEM PARAMETERS

Parameter	Visible[a]	3.6 μm[b]	5.8 μm[b]
$R_p/R_\star$	0.1575 ± 0.0017	0.1560 ± 0.0008 ± 0.0002 (0.8 σ)[c]	0.1541 ± 0.0009 ± 0.0009 (1.4 σ)[c]
b	0.658 ± 0.027	0.656 ± 0.014 ± 0.001 (0.1 σ)[c]	0.638 ± 0.020 ± 0.002 (0.6 σ)[c]
$(R_\star/R_\odot)(M_\star/0.82\ M_\odot)^{-1/3}$	0.753 ± 0.025	0.747 ± 0.011 ± 0.001 (0.2 σ)[c]	0.728 ± 0.016 ± 0.003 (0.8 σ)[c]
T_0[d] (s)	...	53,214 ± 9 ± 2	53,218 ± 11 ± 5

[a] From Winn et al. 2007.
[b] This work; both statistical and systematic uncertainties are given.
[c] Deviation from values in the visible.
[d] Given as $T_{\rm UTCS} - 215{,}500{,}000$ s.

responding to the extreme values of t_s, we thus set the value of each parameter, in each channel, to the mean of each sample of solutions. The uncertainties on the obtained values should reflect the dispersion observed. Therefore, we set a systematic error bar on each parameter, equal to the standard deviation in each sample of solutions.

4. RESULTS AND DISCUSSION

The quality of the method is confirmed by the good agreement between system parameters independently obtained with the best fits to the light curves at both wavelengths (see Fig. 3; the values are reported in Table 1). We measure consistent planet-to-star radius ratios of $0.1560 \pm 0.0008(\text{stat}) \pm 0.0002(\text{syst})$ and $0.1541 \pm 0.0009(\text{stat}) \pm 0.0009(\text{syst})$, at 3.6 and 5.8 μm, respectively. Using the notation introduced above, we find $\Delta_R(\text{obs}) = -0.84 \pm 1.00(\text{stat}) \pm 0.84(\text{syst})\%$.

Tinetti et al. (2007a, 2007b) estimated that the presence of H_2O in the atmosphere of the planet would result in a radius at 5.8 μm being $\Delta_R(H_2O) \sim 0.85\%$–$1.7\%$ larger than at 3.6 μm. Our result is 0.9 σ away from the lower bound of the predictions interval; it is 1.4 σ away from the upper bound. The present results are also significantly different from those of Tinetti et al. (2007b), which are obtained from a preliminary analysis of the same data set. The difference is mainly due to several effects taken into account and discussed in the present work: the bandwidth effect, the determination of the light curve baseline, and the limb darkening. All these effects have the same order of magnitude as the predicted H_2O absorption and could cause a false positive detection. In particular, the limb darkening—in this system with a large b—makes the occultation depth $\Re' \neq (R_p/R_\star)^2$ and impacts on the error budget. Since this effect also depends on the wavelength, it is inaccurate to base the detection of an atmospheric signature only on the raw difference of occultation depths.

Most recent radius measurements for HD 189733b are plotted in Figure 4. A particular comparison between the system parameters we derived in the IR and those derived by Winn et al. (2007) shows that R_p, b, and $R_\star$ values at 3.6 and 5.8 μm are consistent with the visible values (see Table 1). Our two radius measurements are also compatible with the value derived at 8 μm by Knutson et al. (2007b), which has a rather small uncertainty compared to ours. Our statistical uncertainty is of the same order as the one derived by Winn et al. (2007). During the last stage of the publication of this work, new measurements in the visible have been reported by Pont et al. (2007) using the *Hubble Space Telescope*. Their derived system parameters are within 1–2 σ from ours; this marginal disagreement might be explained by stellar spots in such an active K-type star observed at different epochs.

More generally, the consistency between visible and IR radii for other extrasolar planets—for example, HD 209458b, measured in the visible by Knutson et al. (2007a) and at 24 μm by Richardson et al. (2006), or GJ 436b, measured in the visible by Gillon et al. (2007a) and at 8 μm by Gillon et al. (2007b) and Deming et al. (2007)—shows that we do not yet achieve radius determination with enough accuracy in the IR to allow for a spectroscopic characterization of Icarian atmospheres.[3] The accuracy required ($\sim 10^{-4}$) could be obtained by observing several transits with the longest possible out-of-transit baseline, in order to better constrain the systematics in the transit curve. New *Spitzer*/IRAC observations of HD 189733b at 3.6, 4.5, and 8 μm should allow the present results to be better constrained.

We thank the anonymous referee who greatly contributed to improving the Letter, as well as S. Carey and V. Meadows for their help. D. K. S. is supported by CNES. This work is based on observations made with the *Spitzer Space Telescope*, which is operated by the Jet Propulsion Laboratory, California Institute of Technology, under a contract with NASA.

[3] From Icarus (*Ικαρος*), who flew too close to the Sun; i.e., "close-in atmospheres."

REFERENCES

Bakos, G. Á., et al. 2006, ApJ, 650, 1160
Ballester, G. E., Sing, D. K., & Herbert, F. 2007, Nature, 445, 511
Barman, T. 2007, ApJ, 661, L191
Bouchy, F., et al. 2005, A&A, 444, L15
Brown, T. M. 2001, ApJ, 553, 1006
Charbonneau, D., Brown, T. M., Noyes, R. W., & Gilliland, R. L. 2002, ApJ, 568, 377
Deming, et al. 2007, ApJ, submitted (arXiv:0707.2778)
Fazio, G. G., et al. 2004, ApJS, 154, 10
Fortney, J. J., & Marley, M. S. 2007, ApJ, 666, L45
Gillon, M., et al. 2007a, A&A, in press (arXiv:0705.2219)
———. 2007b, A&A, submitted (arXiv:0707.2261)
Hébrard, G., & Lecavelier des Etangs, A. 2006, A&A, 445, 341
Hébrard, G., et al. 2002, ApJS, 140, 103
Horne, K. 1986, PASP, 98, 609
Knutson, H. A., Charbonneau, D., Noyes, R. W., Brown, T. M., & Gilliland, R. L. 2007a, ApJ, 655, 564
Knutson, H. A., et al. 2007b, Nature, 447, 183
Kurucz, R. 2006, Stellar Model and Associated Spectra, http://kurucz.harvard.edu/grids.html
Mandel, K., & Agol, E. 2002, ApJ, 580, L171
Morales-Calderón, et al. 2006, ApJ, 653, 1454
Naylor, T. 1998, MNRAS, 296, 339
Pont, F., et al. 2007, A&A, submitted (arXiv:0707.1940)
Reach, W. T., et al. 2006, IRAC Data Handbook ver. 3.0, http://ssc.spitzer.caltech.edu/irac/dh/iracdatahandbook3.0.pdf
Richardson, L. J., Harrington, J., Seager, S., & Deming, D. 2006, ApJ, 649, 1043
Tinetti, G., Liang, M.-C., Vidal-Madjar, A., Ehrenreich, D., Lecavelier des Etangs, A., & Yung, Y. L. 2007a, ApJ, 654, L99
Tinetti, G., et al. 2007b, Nature, 448, 169
Vidal-Madjar, A., Lecavelier des Etangs, A., Désert, J.-M., Ballester, G. E., Ferlet, R., Hébrard, G., & Mayor, M. 2003, Nature, 422, 143
Vidal-Madjar, A., et al. 2004, ApJ, 604, L69
Winn, J. N., et al. 2007, AJ, 133, 1828